



Preparation of ordered mesoporous carbons containing well-dispersed and highly alloying Pt–Co bimetallic nanoparticles toward methanol-resistant oxygen reduction reaction

Shou-Heng Liu*, Feng-Sheng Zheng, Jyun-Ren Wu

Department of Chemical and Materials Engineering, National Kaohsiung University of Applied Sciences, Kaohsiung 80778, Taiwan

ARTICLE INFO

Article history:

Received 28 February 2011

Received in revised form 9 August 2011

Accepted 11 August 2011

Available online 19 August 2011

Keywords:

PtCo alloy

Ordered mesoporous carbons

Oxygen reduction reaction

Methanol tolerance

XANES/EXAFS

ABSTRACT

A simple route is described for the synthesis of well-dispersed and highly alloying PtCo bifunctional nanoparticles supported on ordered mesoporous carbons (Pt_{100-x}Co_x/OMC) by the simultaneous pyrolysis of carbon and metal precursors in a mesoporous silica as the hard template. A variety of different spectroscopic and analytical techniques was used to thoroughly characterize the Pt_{100-x}Co_x/OMC samples. By X-ray diffraction, N₂ adsorption/desorption isotherms and transmission electron microscopy, it was found that Pt_{100-x}Co_x/OMC possessed well-dispersed Pt/PtCo nanoparticles (2–3 nm) supported on high surface area (~1000 m² g⁻¹) and regular pore channels (~2.8 nm). Among Pt_{100-x}Co_x/OMC catalysts, the Pt₅₀Co₅₀/OMC was found to have superior electrocatalytic activity and the tolerance to methanol crossover during oxygen reduction reaction as compared to typical commercial electrocatalysts. This may be attributed to the dispersion and unique nanostructure of highly alloyed PtCo nanoparticles supported on Pt₅₀Co₅₀/OMC evidenced by X-ray absorption spectroscopy.

© 2011 Elsevier B.V. All rights reserved.

1. Introduction

Direct methanol fuel cells (DMFCs) and polymer electrolyte membrane fuel cells (PEMFCs) have been considered as two of next-generation electrical power sources for light-duty vehicles and stationary or portable applications [1–3] as an alternative to conventional power sources, for example, internal combustion engines and secondary batteries [4–6]. For the past few years, much effort from government, industry, and academy has been devoted to developing DMFCs/PEMFCs and great advances have been achieved; however, the remaining barriers to widespread use are including (i) the high costs of Pt-based electrocatalysts [7–9], (ii) the poor kinetics of both anode and cathode reactions [10,11], (iii) durability of carbon supported catalysts [12–14] and (iv) the crossover of methanol from the anode to the cathode through the proton exchange membranes [15–17]. In terms of the first two problems, progressive increase on price of Pt that is the active species in the most of the presently used electrocatalysts requires a decrease in the usage of Pt and/or an increase in the mass specific activity of the active species. Thus, supporting materials with high surface area conducive to Pt dispersion, proper textural properties favor to kinetics of both anode and cathode reactions, and

high electronic conductivity are highly desirable [18]. With respect to the last two ones [19–22], structural stability and surface properties of the catalyst supports as well as the methodologies invoked in incorporating Pt catalyst onto the support are crucial for the dispersion and stability of the metal nanoparticles during DMFCs/PEMFCs operations in terms of eliminating CO-poisoning and methanol crossover [23,24] at anode and cathode, respectively.

Recently, alloying of Pt with transition metals such as Fe [25,26], Co [27–29], Ni [30,31] and Cr [32] catalysts has been intensively studied and shown enhanced activity toward oxygen reduction reaction (ORR) and high tolerance toward methanol crossover. In general, alloyed catalysts should be performed at high temperatures to assist the formation of alloy metal components. PtCo alloy supported electrocatalysts for ORR have been also prepared via the addition of Co species onto carbon-supported Pt metal catalysts and then alloying at high temperatures more than 973 K in inert gas or hydrogen [33,34]. However, the alloyed particles so fabricated easily aggregate to form larger particles during treatment at high temperatures. To circumvent this problem, Pt-based alloy catalysts for the ORR in DMFCs/PEMFCs are then prepared by the reduction of metal precursors with chemical reductants such as NaBH₄ at low temperatures in place of catalyst treatment at high temperatures under hydrogen flow [35–37]. Nevertheless, the alloying degree of the metal catalysts prepared in this way is generally relatively low. It is well-known that the catalytic performance of the alloyed catalysts strongly depends on their metal particle size and alloying

* Corresponding author. Tel.: +886 7 381 4526x5152; fax: +886 7 3830674.

E-mail address: shliu@kuas.edu.tw (S.-H. Liu).

degree. Thus, there are still high demands to explore new preparation methods to attain the alloyed particles with a uniformly small size and a high alloying degree.

Here we report a novel procedure for the synthesis of an ordered mesoporous carbon with well-dispersed and highly alloying PtCo nanoparticles (denoted as Pt_{100-x}Co_x/OMC, $x = 0, 30$ and 50) based on the simultaneous pyrolysis of furfuryl alcohol, Pt and Co precursors with different Pt/Co atomic ratios in a mesoporous silica, namely SBA-15. Among Pt_{100-x}Co_x/OMC samples, the Pt₅₀Co₅₀/OMC catalysts so fabricated possess not only high activity but also durability (tolerance to methanol crossover) favorable for ORR and hence should render future practical applications as supported cathodic electrocatalysts for DMFCs and PEMFCs.

2. Experimental method

2.1. Preparation of catalysts

The template (SBA-15 mesoporous silica) was synthesized according to the procedure reported in the literature [38]. Subsequent direct replication of SBA-15 template into mono (Pt₁₀₀/OMC) and bifunctional (Pt_{100-x}Co_x/OMC) samples with various relative metal loading was accomplished by the stepwise method as below. Typically, ca. 0.5 g of calcined SBA-15 was first dehydrated at 673 K for 4 h under vacuum while various amounts of platinum acetylacetonate (Pt(CH(COCH₃)₂)₂), denoted as Pt(acac)₂ (98%, Acros) and cobalt acetylacetonate (Co(CH(COCH₃)₂)₂), denoted as Co(acac)₂ (99%, Acros) were co-dispersed in furfuryl alcohol (FA; 98%, Acros) and trimethylbenzene (TMB; 98%, Acros) under ultrasonication. In addition, the FA and TMB solution were polymerized by the addition of oxalic acid (98%, Acros). The mixture solution was then infiltrated in SBA-15 at room temperature (298 K) by an incipient wetness impregnation method, followed by polymerization first at 333 K then at 353 K each for 12 h in air. The resultant composite was increased the temperature to 1073 K with a heating rate of 1 K/min and eventually maintained at the same temperature for 3 h under vacuum. Finally, the resultant black powders were leached with HF (1 wt.%) aqueous solution for at least 24 h to remove the silica template, washed with distilled water and alcohol, then dried at 373 K to obtain the Pt₁₀₀/OMC and Pt_{100-x}Co_x/OMC samples.

2.2. Characterization methods

X-ray diffraction (XRD) patterns of all samples were recorded on a PANalytical (X'Pert PRO) instrument using Cu-K α radiation ($\lambda = 0.1541$ nm). The compositions of catalysts were measured by energy dispersive X-ray analysis (EDX, JEOL JEM-2100F). X-ray photoelectron spectra (XPS) were acquired through an energy analyzer with a constant pass energy of 20 eV followed by irradiating a sample pellet (6 mm in diameter) with a monochromatic Al-K α (1486.6 eV) X-ray under ultra-high vacuum condition (10^{-10} Torr). Nitrogen adsorption isotherms were measured at 77 K on a Micromeritics ASAP 2020 analyzer. For the high-resolution transmission electron microscopy (TEM), samples were first suspended in acetone (99.9 vol.%) by ultrasonication, followed by deposition of the suspension on a lacey carbon grid, then the TEM images were obtained at room temperature using an electron microscope (JEOL JEM-2100F) operating at an electron acceleration voltage of 200 kV. The Pt L_{III}-edge and Co K-edge XANES and EXAFS spectra of the Pt_{100-x}Co_x/OMC samples were collected at the Wiggler beamlines 17C of the National Synchrotron Radiation Research Center (NSRRC) in Taiwan. A Si(1 1 1) double-crystal monochromator was used for selection of energy with a resolution of 2×10^{-4} eV/eV. Two gas-filled ionization chambers were used in series to measure the intensities of the incident beam (I_0) and the beam transmitted

through the sample (I_t) on a reference foil (I_r). A third ion chamber was used in conjunction with a reference sample (Pt foil or Co powder for Pt L_{III}-edge or Co K-edge measurements, respectively). Standard procedures were employed to analyze the spectra acquired by X-ray absorption spectroscopy (XAS). Each EXAFS function (χ) was obtained by subtracting the post-edge background from the overall absorption and then normalized with respect to the edge jump step. Subsequently, k^2 -weighted $\chi(k)$ spectra in the k -space, ranging respectively from 3.6 to 13.8 Å⁻¹ for Pt L_{III}-edge and from 3.6 to 11.5 Å⁻¹ for Co K-edge, were Fourier transformed (FT) to the r -space to separate the EXAFS contributions from different coordination shells. A nonlinear least-squares algorithm was applied to fit (without phase correction) the EXAFS spectra in the r -space between 1.5 and 3.2 Å for Pt and between 1.3 and 3.1 Å for Co, respectively. The Pt–Co reference file was determined by theoretical calculation. All computer programs were implemented in an UWXAFS 3.0 package [39] with the backscattering amplitude and the phase shift for the specific atom pairs being theoretically calculated using the FEFF7 code [40].

2.3. Electrochemical measurements

The electrocatalytic measurements were performed in a single compartment glass cell with a standard three-electrode configuration. A glassy carbon electrode with a diameter of 5 mm was used as a working electrode and a saturated Ag/AgCl electrode and a platinum wire were used as reference and counter electrodes, respectively. The glassy carbon thin-film electrode was prepared by the following steps: firstly, ca. 5 mg of Pt/PtCo-loaded carbon sample was added into 2.5 mL deionized water, followed by ultrasonic treatment for 0.5 h. Then, ca. 20 μ L of the resultant suspension mixture was withdrawn and injected onto the glassy carbon electrode, followed by drying in air at 333 K for 1 h. Finally, 20 μ L of 5% Nafion® (DuPont) solution was added as a binder under N₂ environment. Electrocatalytic activity measurements of various samples and a commercial Johnson-Matthey Pt/C sample (20 wt.% Pt on Vulcan XC-72, denoted as JM-Pt/C) were performed on a galvanostat/potentiostat (CHI Instruments, 727D). Cyclic voltammetry (CV) experiments were done to clean and activate the electrode surface. Prior to each CV measurement, the electrolytic solution was purged with high-purity N₂ (99.9%) for at least 0.5 h to remove the dissolved oxygen, subsequently the experiment was conducted between -0.2 and 1.0 V vs. Ag/AgCl under purging N₂ condition. ORR was evaluated by a linear sweep voltammetry (LSV) technique. The 0.5 M H₂SO₄ electrolyte was saturated with ultrahigh purity oxygen for at least 0.5 h. The polarization curves were obtained between -0.1 and 0.8 V vs. Ag/AgCl at a scanning rate of 5 mV/s and a rotating speed of 1600 rpm under room temperature condition. Accelerated durability tests (ADT) of Pt₅₀Co₅₀/OMC and JM-Pt/C samples were performed by cycling the electrode potential between -0.2 and 1.0 V vs. Ag/AgCl at a scanning rate of 50 mV/s for 1000 cycles in a nitrogen-saturated atmosphere over a period of 13 h.

Single cell tests were carried out in a 5 cm² cross-sectional catalyst area (2.25 cm \times 2.25 cm). Various catalyst inks containing Nafion ionomer (DuPont, 5 wt.% solution), electrocatalysts, and isopropyl alcohol were applied on carbon cloth substrates (APWOS1002). Pt loading was 0.2 and 0.4 mg/cm² for the anode and cathode, respectively. A Nafion 212 membrane (DuPont) was inserted between the anode and cathode layers by hot pressing at 398 K under a pressure of 50 kg/cm². The hydrogen and air were used as the fuels with the flow rates of 300 and 2000 mL/min, respectively. The gases were humidified at a relative humidity of 100%. The cells were operated at 353 K and the operating pressure was atmospheric. Prior to the measurement, cells were activated

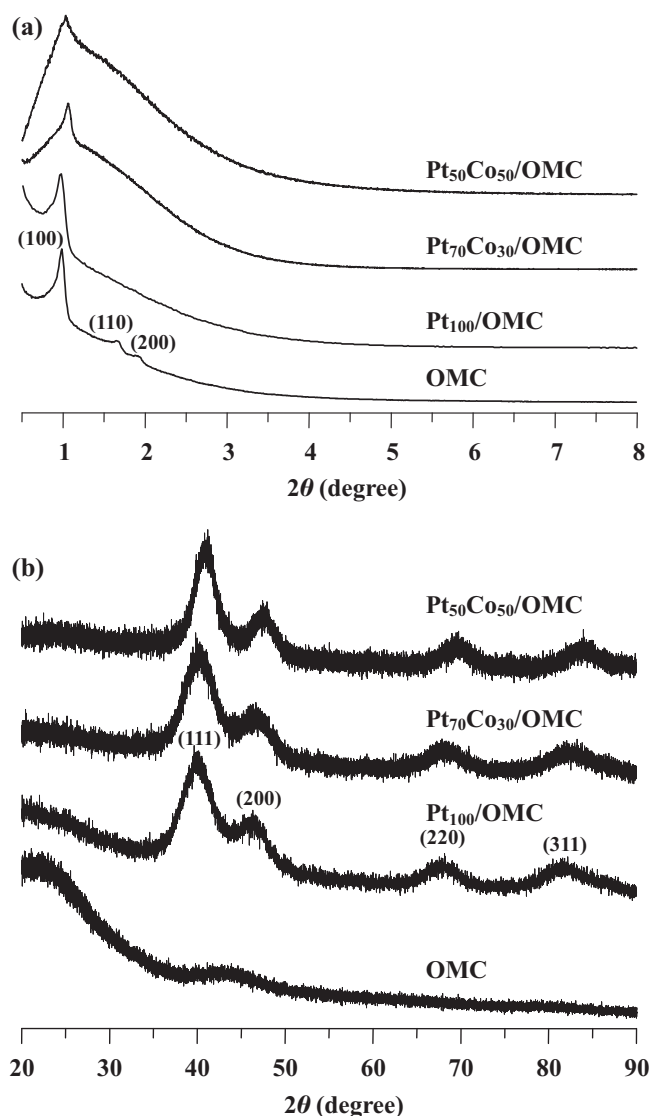


Fig. 1. (a) Small- and (b) large-angle powdered XRD patterns of various samples.

by polarization at a constant current until stable performance was obtained.

3. Results and discussion

As displayed in Fig. 1a, the small-angle XRD pattern of OMC samples show a main (1 0 0) diffraction peak at $2\theta \approx 1.0^\circ$ and two weak features (1 1 0) and (2 0 0) at $2\theta \approx 1.6^\circ$ and 1.8° , respectively, indicating the existence of a mesoporous structure with a long-range order and a two-dimensional hexagonal symmetry similar to that of the ordered mesoporous carbon (CMK-3) [41]. However, upon incorporation of Pt and Pt/Co into the pristine OMC sample, less resolved higher order (1 1 0) and (2 0 0) diffraction peaks were observed, implying that the presence of metals has resulted in lacking a long-range structural ordering of mesopores. Also, it is noted that variations in Pt/Co loading indeed have some influence on the overall structure and the physical properties of the catalyst since a decrease in the unit cell parameter (a) of the 2-D hexagonal lattice of $\text{Pt}_{100-x}\text{Co}_x/\text{OMC}$ samples was found (Table 1) compared to the pristine OMC. In addition, the large-angle XRD pattern of $\text{Pt}_{100}/\text{OMC}$ (see Fig. 1b) shows distinct (1 1 1), (2 0 0), (2 2 0), and (3 1 1) diffraction peaks at $2\theta = 39.8^\circ$, 46.2° , 67.8° , and 81.3° , respectively, indicating that the Pt metal particle has a face-

centered cubic (fcc) structure. Upon increasing the Co loading, all the $\text{Pt}_{100-x}\text{Co}_x/\text{OMC}$ samples exhibit diffraction patterns that are similar to that of the $\text{Pt}_{100}/\text{OMC}$ catalyst, except that the 2θ values of their main peak was slightly shifted toward a higher value, suggesting a reduction of their respective lattice constants (a_{fcc} ; see Table 1) [42] and hence an increasing extent of the alloying of the Pt and Co particles in the OMC supports [43]. The average metal particle sizes (D_p) of $\text{Pt}_{100-x}\text{Co}_x/\text{OMC}$ samples deduced from the Scherrer formula are shown in Table 1. Increasing substitution of Pt by the Co atoms in $\text{Pt}_{100-x}\text{Co}_x/\text{OMC}$ samples was found to have insignificant impacts on the PtCo alloyed particle size. Moreover, the XRD pattern observed for $\text{Pt}_{100-x}\text{Co}_x/\text{OMC}$ samples did not match with the typical hexagonal close-packed (hcp) structure of pure Co and Co oxide, indicating that some cobalt oxides may be present as an amorphous state in $\text{Pt}_{100-x}\text{Co}_x/\text{OMC}$. Nonetheless, the absence of the hcp phase of Co in $\text{Pt}_{100-x}\text{Co}_x/\text{OMC}$ samples confirms the formation of PtCo alloys in the supported catalysts.

All the N_2 adsorption/desorption curves of OMC and $\text{Pt}_{100-x}\text{Co}_x/\text{OMC}$ samples showed the typical type-IV isotherm with a well-defined hysteresis loop (see Fig. S1a in the supporting information). Consequently, the BET surface area, pore volume, and pore size distribution (by BJH method) of various samples can be derived. As can be summarized in Table 1, all supported catalyst samples were found to possess a high surface area ($\sim 1000 \text{ m}^2/\text{g}$) and a uniform pore size distribution (2.6–2.9 nm; Fig. S1b). The average pore size observed for various $\text{Pt}_{100-x}\text{Co}_x/\text{OMC}$ samples is comparable to the pristine OMC which is due to the fact that they arise from the skeleton of the SBA-15 mesoporous silica template, which was subsequently removed by HF washing after carbonization. Nevertheless, the surface areas and pore volumes of $\text{Pt}_{100-x}\text{Co}_x/\text{OMC}$ samples are smaller than those of pristine OMC, which may be owing to partial exposure of the PtCo nanoparticles (after silica template removal) and the higher density of the alloyed metal than OMC.

The structure and metal dispersion of $\text{Pt}_{100-x}\text{Co}_x/\text{OMC}$ samples were further confirmed by TEM measurements. Fig. 2 presents the TEM images for three $\text{Pt}_{100-x}\text{Co}_x/\text{OMC}$ samples, together with the particle size distribution histograms. The Pt/PtCo particle size distribution was estimated by measuring the size of at least one hundred randomly chosen particles in the magnified TEM images. As shown in Fig. 2, the $\text{Pt}_{100}/\text{OMC}$, $\text{Pt}_{70}\text{Co}_{30}/\text{OMC}$ and $\text{Pt}_{50}\text{Co}_{50}/\text{OMC}$ samples exhibit an ordered array of mesoporous carbon nanorods dispersed with uniform Pt and PtCo nanoparticles with average sizes of 2.2, 2.5 and 3.0 nm, respectively. The average particle sizes calculated by TEM are in agreement with those obtained by XRD, as shown in Table 1. The histograms of metal particle size distribution shown in Fig. 2 also indicate a uniform and narrower distribution of Pt and PtCo particle morphology. This indicates that the well-defined mesostructures of $\text{Pt}_{100-x}\text{Co}_x/\text{OMC}$ samples facilitate a confined effect for the Pt/PtCo nanoparticles, most likely due to the restricted Ostwald ripening and/or migration-coalescence of Pt particles in these structures, as observed for the systems of Au nanoparticles incorporated mesoporous silicas [44,45].

The structural features and the chemical oxidation states of C, O, Pt and Co, in the $\text{Pt}_{100-x}\text{Co}_x/\text{OMC}$ samples with various Pt/Co atomic ratios were characterized by XPS analysis. As can be seen in Fig. S2a, all the C 1s XPS spectra obtained from the $\text{Pt}_{100-x}\text{Co}_x/\text{OMC}$ samples revealed a broad peak centered at ca. 284.5 eV, which could be attributed to the sp^2 graphitic carbon species. Compared to graphitized carbon black (0.82 eV) [46,47], a similar full-width half-maximum (FWHM) linewidth of ca. 1.3 eV was observed in all the C 1s spectra for $\text{Pt}_{100-x}\text{Co}_x/\text{OMC}$ samples, suggesting the presence of less ordered graphene layers. Again, this may be attributed to perturbation of the embedded Pt or PtCo alloys in the OMC frameworks. Similarly, all the O 1s spectra (see Fig. S2b in the supporting information) showing single broad peaks

Table 1
Textural properties of pure OMC and various Pt_{100-x}Co_x/OMC samples.

Sample	Pt/Co ^a	<i>a</i> (nm) ^b	<i>S</i> _{BET} (m ² /g) ^c	<i>d</i> _{BJH} (nm) ^d	<i>V</i> _{tot} (cm ³ /g) ^e	<i>D</i> _p (nm) ^f	<i>a</i> _{fcc} (nm) ^g
OMC	–	10.6	1596	2.9	1.19	–	–
Pt ₁₀₀ /OMC	8/0	10.5	1091	2.8	0.77	2.5	0.3904
Pt ₇₀ Co ₃₀ /OMC	8/1	10.1	955	2.8	0.97	2.6	0.3876
Pt ₅₀ Co ₅₀ /OMC	8/2.5	10.1	778	2.6	0.81	3.0	0.3839

- ^a Metal atomic ratios (wt.%/wt.%) deduced from EDX results.
^b Unit cell parameters of the ordered mesoporous carbon support.
^c Brunauer–Emmet–Teller (BET) surface areas.
^d Pore diameters calculated by the Barrett–Joyner–Halenda (BJH) method using the adsorption branches.
^e Total pore volumes calculated as the amount of N₂ adsorbed at a relative pressure of 0.99.
^f Average particle size deduced by Scherrer formula.
^g Lattice constants of Pt and PtCo alloys deduced by Vegard's Law based on the (2 2 0) diffraction peak in Fig. 1b.

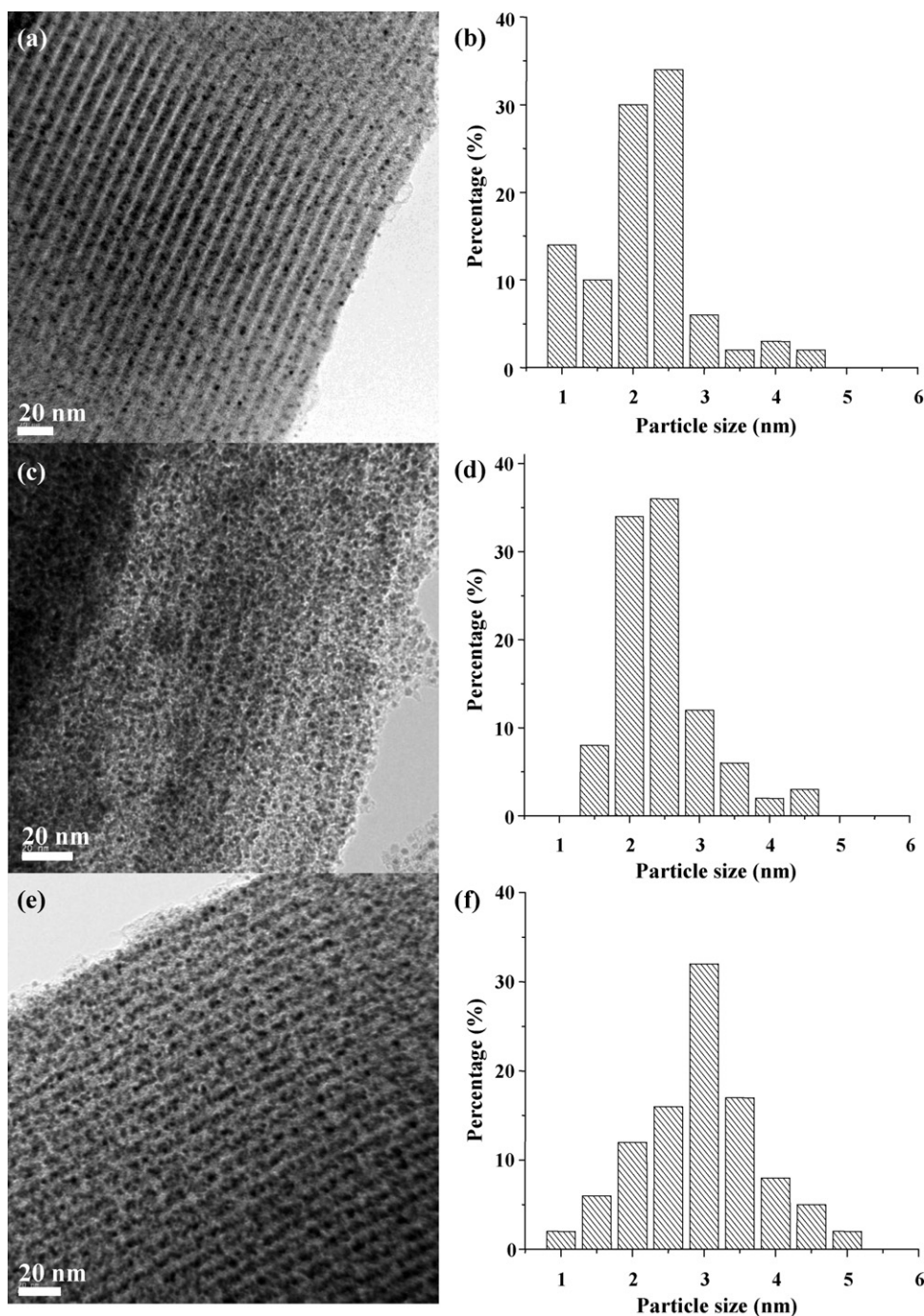


Fig. 2. TEM images and histograms of Pt and PtCo particle size distributions of (a) and (b) Pt₁₀₀/OMC (c) and (d) Pt₇₀Co₃₀/OMC (e) and (f) Pt₅₀Co₅₀/OMC samples.

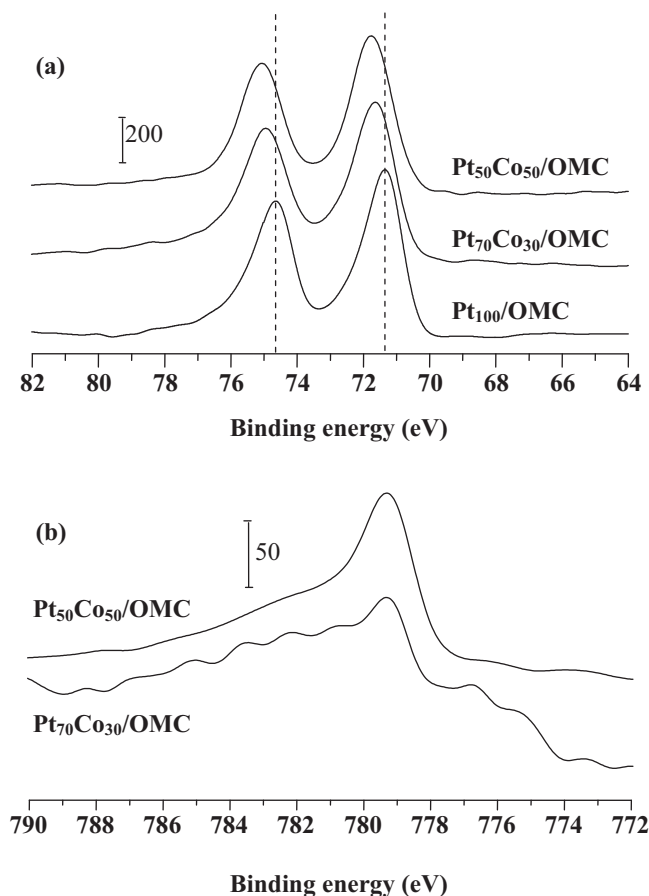


Fig. 3. XPS spectra of various samples at the (a) Pt 4f and (b) Co 2p regions.

indicate the existence of different oxygen species. The Pt 4f spectra of Pt₁₀₀/OMC in Fig. 3a show two broad peaks, which could be deconvoluted into two pairs of doublets with the most intense peaks centering at binding energies of ca. 71.4 and 74.7 eV, respectively. These two intense peaks are attributed to Pt 4f_{7/2} and Pt 4f_{5/2} excitations of metallic Pt(0), while the two weaker shoulder peaks (at 72.3 and 75.6 eV) are ascribed to oxidized platinum, i.e., Pt(II). Compared with Pt₁₀₀/OMC, two intense peaks attributed to Pt(0) for the Pt₇₀Co₃₀/OMC and Pt₅₀Co₅₀/OMC samples were found to positively shift toward higher binding energies, probably due to stronger Pt–Co interactions on the carbon support [48]. Likewise, the Co 2p_{3/2} XPS spectra (Fig. 3b) could be deconvoluted into two peaks with binding energies of ca. 780 and 778 eV which were assigned as Co(II) and Co metal, respectively. Thus, it is indicative that the surface of the PtCo nanoparticles on various Pt_{100–x}Co_x/OMC samples is mainly composed of Pt(0) metals and Co oxides. Similar observations were found in the PtRu alloys system [49–51] that the presence of oxygen species in Ru oxides has been suggested [52] to play a bifunctional role for CO and methanol oxidation reactions under normal DMFC operations.

To further understand the structure and the extent of the alloying of PtCo nanoparticles in the Pt_{100–x}Co_x/OMC samples, additional X-ray absorption spectroscopy (XAS) experiments were performed using a synchrotron radiation light source. The electronic properties of the PtCo nanoparticles supported OMC were studied by X-ray absorption near edge structure (XANES) analyses. Fig. 4a shows the Pt L_{III} edge XANES of the Pt_{100–x}Co_x/OMC samples and reference Pt foil. The absorption at 11,564 eV is assigned to 2p_{3/2} to 5d electronic transition of Pt metal and its corresponding magnitude of the absorption hump is defined as white line. The white line intensity of the Pt₁₀₀/OMC samples are higher compared

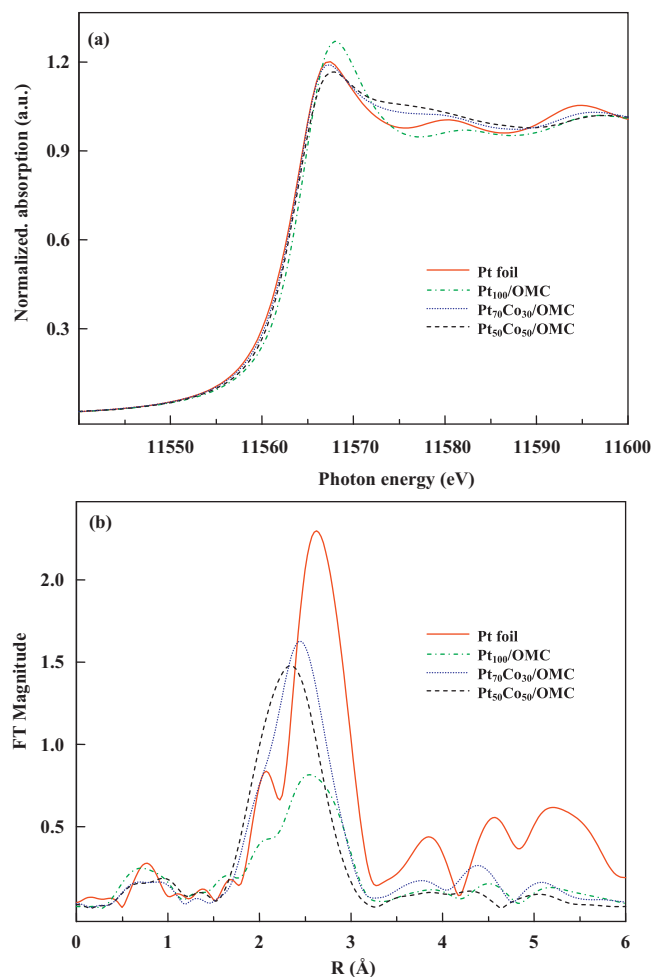


Fig. 4. (a) Pt L_{III}-edge XANES spectra of various samples and (b) Fourier transform magnitudes k^2 -weighted $\chi(k)$ Pt L_{III}-edge EXAFS spectra.

to that of pure Pt foil which may be due to the nanosized effect of Pt particles supported on OMC. On the contrary, the white line intensities of the Pt₇₀Co₃₀/OMC and Pt₅₀Co₅₀/OMC samples are lower than that of pure Pt foil, indicating that the alloying of Co with Pt metal results in more occupied Pt 5d electronic states. Nevertheless, the profiles of the absorption edges for all Pt_{100–x}Co_x/OMC are similar to that of Pt foil, implying the metallic property of Pt in the PtCo nanoparticles of Pt_{100–x}Co_x/OMC. Fig. 4b shows the Fourier Transform (FT) results of the EXAFS oscillations obtained for Pt L_{III} edge of all the Pt_{100–x}Co_x/OMC samples and the Pt foil. The diversity of EXAFS signals at the Pt L_{III}-edge obtained for the Pt foil and the Pt_{100–x}Co_x/OMC samples demonstrate that the absorbing Pt atoms in all samples have different environments in comparison with pure Pt. A peak observed for these samples in the FT spectra ranging from 2.0 to 3.0 Å is owing to the contributions from the first Pt–Co and Pt–Pt coordination shell, again confirming the formation of PtCo alloyed nanoparticles. As listed in Table 2, EXAFS parameters such as the coordination number (N), bond distance (R), Debye–Waller factor (σ^2), and inner potential shift (ΔE_0) were obtained by curve-fitting analyses. A slightly lower Pt–Pt distance was observed for Pt₇₀Co₃₀/OMC (2.650 Å) and Pt₅₀Co₅₀/OMC (2.682 Å) samples compared to the Pt₁₀₀/OMC (2.721 Å) and Pt foil (2.770 Å). This result is comparable to the earlier report [53] observed for commercial JM–PtCo/C catalyst which the Pt–Pt distance of 2.68 Å was found. The lattice contractions owing to PtCo alloying led to a more favorable Pt–Pt spacing for the dissociative adsorption of oxygen [54], resulting in better catalytic activities toward ORR (discussed later).

Table 2
EXAFS structural parameters derived from fitting results at Pt L_{III}-edge and Co K-edge for various Pt_{100-x}Co_x/OMC samples.

Edge	Shell	N ^a	R _j (Å) ^b	σ ² × 10 ⁻³ (Å ²) ^c	ΔE ₀ (eV) ^d	R factor
Pt ₁₀₀ /OMC						
Pt L _{III}	Pt–Pt	6.2	2.721	5.6	3.1	0.002
Pt ₇₀ Co ₃₀ /OMC						
Pt L _{III}	Pt–Co	1.9	2.532	4.6	5.4	0.001
	Pt–Pt	4.8	2.650	6.8	6.5	
Co K	Co–Co	4.2	2.488	6.1	–0.2	
	Co–Pt	1.7	2.532	4.0	–1.8	
Pt ₅₀ Co ₅₀ /OMC						
Pt L _{III}	Pt–Co	1.5	2.655	3.9	4.7	0.012
	Pt–Pt	4.7	2.682	5.6	5.7	
Co K	Co–Co	4.1	2.485	6.0	–0.6	
	Co–Pt	2.1	2.655	4.6	–1.5	

^a N: coordination number.^b R_j: bond distance.^c σ²: Debye–Waller factor.^d ΔE₀: inner potential shift.

Fig. 5a displays the Co K edge XANES spectra for the reference Co foil and Pt_{100-x}Co_x/OMC samples. In term of Co foil, a pre-edge shoulder originating from the 1s to 3d transition is observed at ca. 7709 eV, which is a feature for the tetrahedral site symmetry of cobalt species [55]. However, the pre-edge feature almost disappeared for Pt₇₀Co₃₀/OMC and Pt₅₀Co₅₀/OMC samples, suggesting the formation of the Pt–Co alloy structure by incorporating Co atoms into the Pt lattices. Moreover, the absorption edges of all

Pt_{100-x}Co_x/OMC samples shift toward a higher energy region than that of Co foil, which may be due to the formation of higher oxidation states of Co, i.e., Co oxides in the Pt_{100-x}Co_x/OMC samples. The white line peak centered at ca. 7725 eV ascribes to the 1s to 4p transition in Co foil. As can be seen in Fig. 5a, the white line intensities of the synthesized Pt_{100-x}Co_x/OMC samples are higher than that of the Co foil, which probably caused by the nanosized effect or the formation of Co oxide species. The FT of Co K-edge EXAFS for various samples is shown in Fig. 5b. A peak related to the first coordination shell of Co–Co and Co–Pt was observed at ca. 2.1 Å in the FT spectra for Pt₇₀Co₃₀/OMC samples. However, the main peak of the Pt₅₀Co₅₀/OMC in the FT spectra was slightly shifted toward a longer distance, implying the formation of higher alloying degree of Pt–Co. Similarly, the structure parameters can also be obtained from the EXAFS curve-fitting of Co K-edge, as listed in Table 2.

The extent of alloying could be determined by quantitative analysis of the atomic distribution of PtCo nanoparticles derived from the EXAFS data summarized in Table 3 [33,55,56]. Consequently, the intra-particle dispersion of Pt and Co could be derived by the structural coordination parameters, namely P_{observed} , R_{observed} , $\Sigma N_{\text{Pt-i}}$, $\Sigma N_{\text{Co-i}}$, and Q [57]; as defined and depicted in Table 3. The total coordination number of the Pt and Co atoms around Pt ($\Sigma N_{\text{Pt-i}}$) observed for the Pt₅₀Co₅₀/OMC sample was found to be 6.3; while that around Co ($\Sigma N_{\text{Co-i}}$) was found to be 6.2. The $\Sigma N_{\text{Pt-i}}$ value obtained for the Pt₅₀Co₅₀/OMC sample is almost equal to the corresponding $\Sigma N_{\text{Co-i}}$ value (i.e., $Q = 1.01$), suggesting that nearly all of the Pt and Co atoms were involved in the alloying process. As a result, the Pt and Co atoms in the Pt₅₀Co₅₀/OMC sample observed in this study are tightly coupled through strong heterometallic bonding which leads to the formation of ‘heteroatomic-rich’ nanoclusters [58,59], indicating a higher extent of Pt and Co alloying. On the contrary, the $\Sigma N_{\text{Pt-i}}$ value of Pt₇₀Co₃₀/OMC was greater than the $\Sigma N_{\text{Co-i}}$ value ($Q = 1.14$; see Table 3), indicating that Co atoms are segregated to the surface of the PtCo nanoparticles and Pt atoms to the core, i.e., resulting in ‘core-shell’ nanoclusters, most probably with an inner core enriched in Pt and an outer shell enriched in Co.

To evaluate the electrocatalytic activities of Pt_{100-x}Co_x/OMC and a commercially available JM-Pt/C (Johnson-Matthey; 20 wt.% Pt on Vulcan XC-72 activated carbon) during ORR, linear scanning voltammetry (LSV) tests was performed in O₂ saturated 0.5 M H₂SO₄ solution at room temperature (298 K). As can be seen in Fig. 6 and Table 4, onset potentials of ca. 0.68 V were observed for the Pt₁₀₀/OMC and Pt₇₀Co₃₀/OMC samples. Nonetheless, a notable increase in onset potential of Pt₅₀Co₅₀/OMC sample (0.73 V) was found, which is surpassing that of the commercial JM-Pt/C catalyst (0.70 V). This may be attributed to unique nanostructure between PtCo nanoparticles and carbon supports as well as higher alloying state of Pt₅₀Co₅₀/OMC, as evidenced by the aforesaid XAS

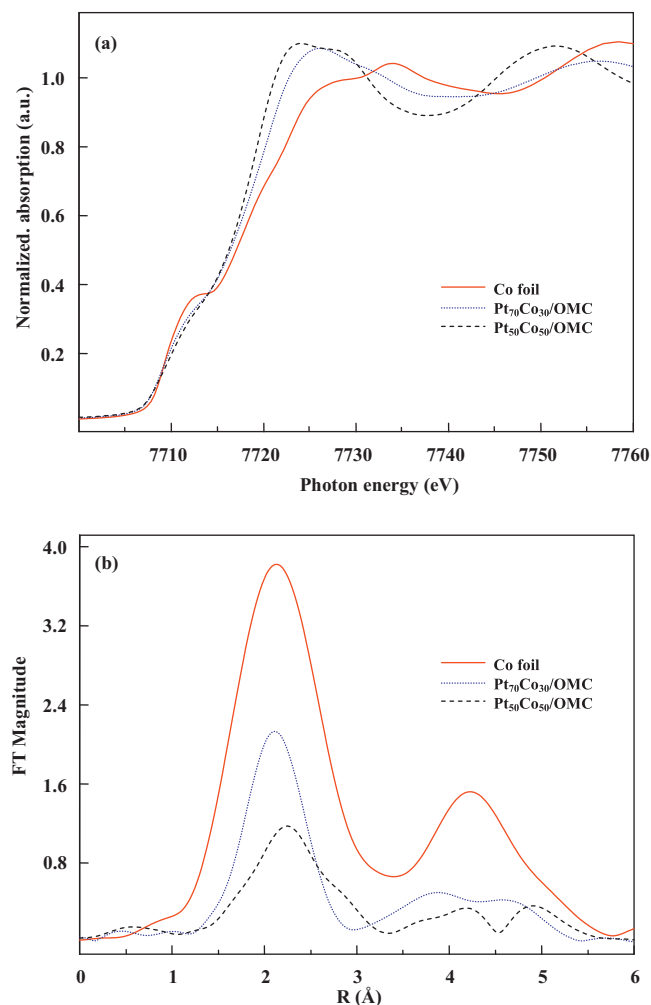
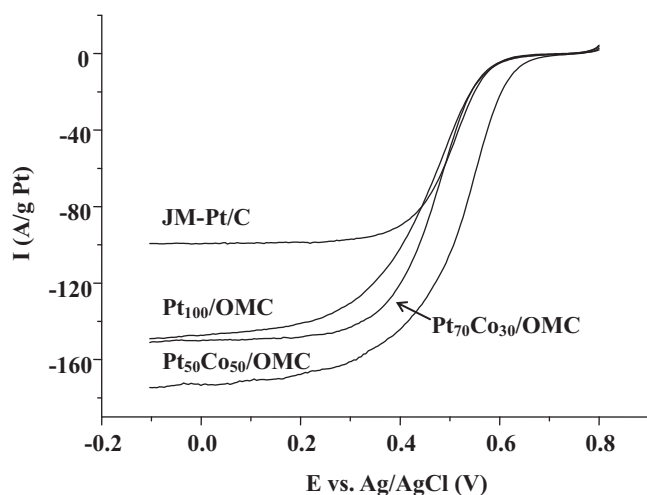


Fig. 5. (a) Co K-edge XANES spectra of various samples and (b) Fourier transform magnitudes k^2 -weighted $\chi(k)$ Co K-edge EXAFS spectra.

Table 3Structural coordination parameters for various Pt_{100-x}Co_x/OMC samples.

Sample	$\Sigma N_{\text{Pt-i}}^{\text{a}}$	$\Sigma N_{\text{Co-i}}^{\text{b}}$	$P_{\text{observed}}^{\text{c}}$	$R_{\text{observed}}^{\text{d}}$	Q^{e}
Pt ₇₀ Co ₃₀ /OMC	6.7	5.9	0.28	0.29	1.14
Pt ₅₀ Co ₅₀ /OMC	6.3	6.2	0.24	0.34	1.01

^a $\Sigma N_{\text{Pt-i}} = N_{\text{Pt-Pt}} + N_{\text{Pt-Co}}$.^b $\Sigma N_{\text{Co-i}} = N_{\text{Co-Co}} + N_{\text{Co-Pt}}$.^c $P_{\text{observed}} = N_{\text{Pt-Co}} / \Sigma N_{\text{Pt-i}}$.^d $R_{\text{observed}} = N_{\text{Co-Pt}} / \Sigma N_{\text{Co-i}}$.^e $Q = \Sigma N_{\text{Pt-i}} / \Sigma N_{\text{Co-i}}$.**Fig. 6.** Polarization curves for the O₂ reduction on various Pt_{100-x}Co_x/OMC and JM-Pt/C in O₂ saturated 0.5 M H₂SO₄ solution at room temperature.

results. It is noted that, unlike the commercial JM-Pt/C catalyst (20 wt.% Pt), the Pt₅₀Co₅₀/OMC catalysts reported herein contain only ca. 8 wt.% Pt and 2.5 wt.% Co (Table 1). Thus, in terms of the production cost and the mass activity of the PtCo catalyst, Pt₅₀Co₅₀/OMC are far superior than JM-Pt/C.

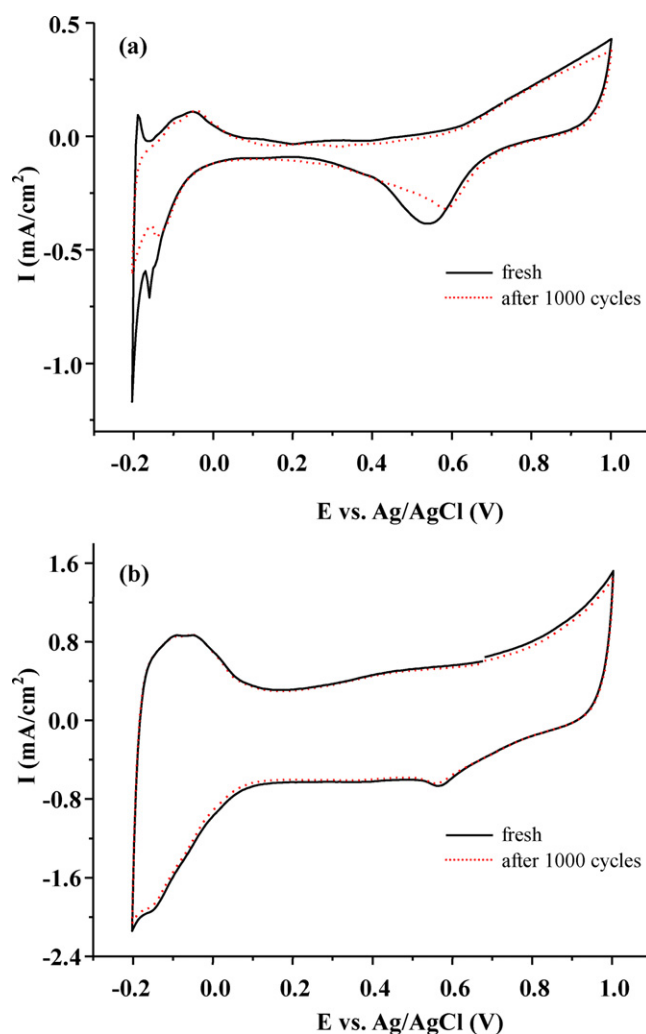
The electrocatalytic durability and tolerance to the methanol crossover at the cathode has been recently recognized as two of the most important issues for fuel cells [60–62]. Thus, accelerated durability tests (ADT) of Pt₅₀Co₅₀/OMC and JM-Pt/C samples were studied by cycling the electrode potential with the appropriate lower (−0.2 V vs. Ag/AgCl) and upper (1.0 V vs. Ag/AgCl) potential limits at a scanning rate of 50 mV/s for 1000 cycles in a nitrogen-saturated atmosphere. As shown in Fig. 7a, the intensities of the peaks attributed to the oxidation–reduction of Pt and desorption–adsorption of hydrogen on Pt metal in the JM-Pt/C were remarkably decreased after repeated 1000 potential cycles. This result indicates that the electrochemical surface area (ECSA) of JM-Pt/C decreased gradually with repeated potential cycling. However, it should be noted that the intensities of the peaks in the cyclic voltammogram for Pt₅₀Co₅₀/OMC (Fig. 7b) remain practically intact over 1000 cycles, indicating the embedded PtCo nanoparticles in the Pt₅₀Co₅₀/OMC indeed possess an electrocatalytic stability during long-term operation.

Table 4Onset potentials and kinetic current densities of various Pt_{100-x}Co_x/OMC and JM-Pt/C samples during the ORR.

Sample	E (V) ^a	I (μA/cm ²) ^b
Pt ₁₀₀ /OMC	0.68	8.6
Pt ₇₀ Co ₃₀ /OMC	0.68	13.3
Pt ₅₀ Co ₅₀ /OMC	0.73	33.3
JM-Pt/C	0.70	15.7

^a Onset potential vs. Ag/AgCl.^b Kinetic current densities at 0.7 V vs. Ag/AgCl.

To further study the methanol-tolerant properties of the synthesized Pt₅₀Co₅₀/OMC electrocatalysts, a series of LSV tests were also carried out to reveal the effect of 0.5 M methanol concentration on electrocatalytic performance of Pt₅₀Co₅₀/OMC as well as the commercially available JM-Pt/C at a rotating speed of 1600 rpm under room temperature. Fig. 8a shows LSV for electrooxidation of methanol on Pt₅₀Co₅₀/OMC and commercial JM-Pt/C catalysts in N₂-saturated 0.5 M H₂SO₄ solution containing 0.5 M CH₃OH. The peak current corresponding to the methanol oxidation reaction on commercial JM-Pt/C catalyst is ca. six times larger than that on the Pt₅₀Co₅₀/OMC catalyst, indicating that the latter one is less active toward methanol oxidation. This could be explained by the hindrance of chemisorption of methanol on the catalyst surface which requires the presence of at least three neighboring Pt atoms in

**Fig. 7.** Cyclic voltammograms for (a) JM-Pt/C and (b) Pt₅₀Co₅₀/OMC during repeated potential cycling in 0.5 M H₂SO₄ at 50 mV s^{−1} under room temperature condition.

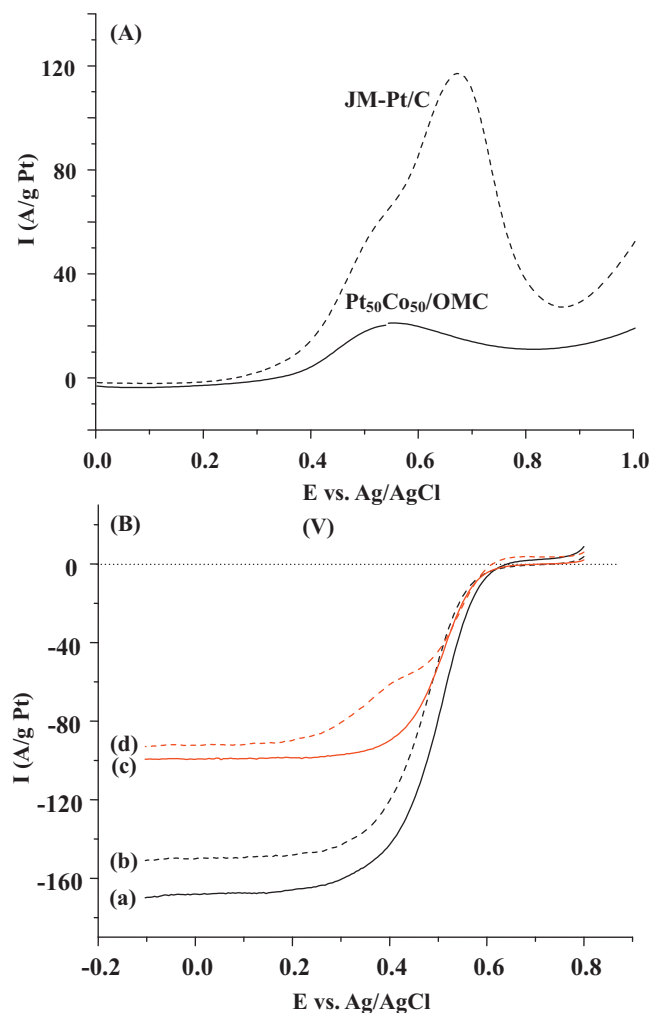


Fig. 8. (A) Linear sweep voltammogram for methanol oxidation on $\text{Pt}_{50}\text{Co}_{50}/\text{OMC}$ and commercial JM-Pt/C catalysts in 0.5 M H_2SO_4 and 0.5 M CH_3OH solution saturated with nitrogen at scan rate of 10 mV s^{-1} . (B) Polarization curves for ORR on $\text{Pt}_{50}\text{Co}_{50}/\text{OMC}$ with (a) 0 M and (b) 0.5 M CH_3OH in O_2 saturated 0.5 M H_2SO_4 solution. Commercial JM-Pt/C for ORR in O_2 saturated 0.5 M H_2SO_4 solution containing (c) 0 M and (d) 0.5 M CH_3OH .

the proper crystallographic orientation [43,63,64]. Further measurements of polarization curves for ORR on $\text{Pt}_{50}\text{Co}_{50}/\text{OMC}$ and JM-Pt/C catalysts were investigated in O_2 saturated 0.5 M H_2SO_4 solution with/without 0.5 M CH_3OH . As shown in Fig. 8b, electrooxidation of methanol by $\text{Pt}_{50}\text{Co}_{50}/\text{OMC}$ was almost not observed between -0.1 and 0.8 V . By contrast, a shoulder at ca. 0.4 V was observed in the polarization curve for JM-Pt/C, indicating the occurrence of methanol oxidation reactions. Owing to the competitive reaction between oxygen reduction and methanol oxidation, the JM-Pt/C showed an increased overpotential during the methanol-containing ORR in comparison with the ORR in pure H_2SO_4 solution. Thus, the JM-Pt/C showed an electrooxidation activity of $5 \text{ A per gram of Pt}$ in a $0.5 \text{ M H}_2\text{SO}_4/0.5 \text{ M CH}_3\text{OH}$ electrolyte at 0.7 V . The surpassing methanol-tolerance during the ORR observed for the $\text{Pt}_{50}\text{Co}_{50}/\text{OMC}$ electrocatalyst, as compared with the JM-Pt/C, can be primarily due to the unique synthesis procedure involving the pyrolysis of co-fed carbon sources and Pt and Co precursors in the nano-channels of SBA-15 template. As shown in Fig. 2, the PtCo nanoparticles in $\text{Pt}_{50}\text{Co}_{50}/\text{OMC}$ were found to be studded and stabilized on the surface of the carbon rods. Consequently, the partial surface of the PtCo nanoparticles was overlaid by carbon films and only accessible to O_2 due to the fact that methanol was hindered

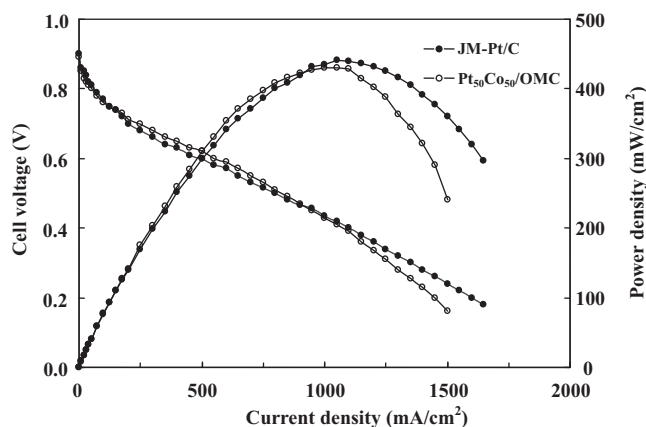


Fig. 9. Performance curves of single cells for $\text{Pt}_{50}\text{Co}_{50}/\text{OMC}$ and the JM-Pt/C as the cathode catalysts at cell operating temperature of 353 K .

from approaching the activity sites because of the carbon films enveloping the PtCo nanoparticles [65]. Moreover, well-alloyed PtCo nanoparticles have been reported to have superior electrocatalytic activity to ORR [56], which may be another contribution to the high performance for the ORR even in the presence of the methanol in the electrolyte.

The performance of single cells at 353 K with $\text{Pt}_{50}\text{Co}_{50}/\text{OMC}$ and JM-Pt/C as cathode catalyst is shown in Fig. 9. The $\text{Pt}_{50}\text{Co}_{50}/\text{OMC}$ was found to have relatively higher power densities at high voltages ($>0.4 \text{ V}$) and lower power densities at low voltages ($<0.4 \text{ V}$) than the commercial Pt/C cathode, indicating that $\text{Pt}_{50}\text{Co}_{50}/\text{OMC}$ possesses surpassing electrocatalytic activity (electrochemical reaction rate). However, the lower power densities observed for the $\text{Pt}_{50}\text{Co}_{50}/\text{OMC}$ catalyst layer at low voltage regions suggest that the mass-transport limitation is greater than that for the commercial Pt/C catalyst layer. It should be noted that most of PtCo nanoparticles supported on the internal surface of OMC (average pore diameter smaller than 3 nm) could barely contact the Nafion electrolyte solution (typically larger than 4 nm) on the external surface of OMC sufficiently (see Fig. S3 in the supporting information). However, these PtCo nanoparticles could touch the oxygen and water vapor presented in the mesoporous channel of OMC easily, due to the interconnection of the pores within OMC. Accordingly, protons may be delivered to PtCo nanoparticles from membrane Nafion phase via water vapor (or water) even if triple-phase-boundary (TPB) is not available for electrocatalytic reaction.

4. Conclusions

The novel $\text{Pt}_{100-x}\text{Co}_x/\text{OMC}$ catalysts reported herein were fabricated by a facile replication method using mesoporous silica as hard templates and by co-feeding carbon sources and metal precursors concurrently during synthesis process. Combined the data from XRD, N_2 adsorption/desorption isotherms and TEM revealing that well-dispersed Pt/PtCo nanoparticles ($2\text{--}3 \text{ nm}$) in the form of a face-centered cubic (fcc) crystalline structure on the $\text{Pt}_{100-x}\text{Co}_x/\text{OMC}$ samples with high surface area and regular pore channels, which facilitate reactant/product diffusion. Results obtained by XPS spectroscopy indicated that PtCo alloy presented on the $\text{Pt}_{50}\text{Co}_{50}/\text{OMC}$ rods were mainly metallic Pt and Co oxides. Further studies by XANES/EXAFS spectroscopies, the $\text{Pt}_{50}\text{Co}_{50}/\text{OMC}$ catalysts, which may be due to the unique nanostructure of well-dispersed and highly alloyed PtCo nanoparticles, were found to have superior electrocatalytic properties and methanol-tolerant stabilities compared to common commercial catalysts during ORR. Thus, the supported $\text{Pt}_{50}\text{Co}_{50}/\text{OMC}$ catalysts so fabricated should render future practical and cost-effective applications in hydrogen-energy

related areas, for example, as electrocatalysts for DMFCs and PEM-FCS.

Acknowledgements

The support of this work by the National Science Council, Taiwan (NSC 99-2221-E-151-044-MY2 and 99-2221-E-151-023-MY2) is gratefully acknowledged. The authors wish to thank Mr. Ding-Goa Liu and Dr. Jyh-Fu Lee (National Synchrotron Radiation Research Center, Taiwan) for their assistance and helpful discussions on the X-ray absorption measurements.

Appendix A. Supplementary data

Supplementary data associated with this article can be found, in the online version, at doi:[10.1016/j.apcatb.2011.08.011](https://doi.org/10.1016/j.apcatb.2011.08.011).

References

- [1] H.A. Gasteiger, S.S. Kocha, B. Sompalli, F.T. Wagner, *Appl. Catal. B: Environ.* 56 (2005) 9–35.
- [2] R.F. Service, *Science* 324 (2009) 1257–1259.
- [3] H. Liu, W. Li, A. Manthiram, *Appl. Catal. B: Environ.* 90 (2009) 184–194.
- [4] R. Borup, J. Meyers, B. Pivovar, Y.S. Kim, R. Mukundan, N. Garland, D. Myers, M. Wilson, F. Garzon, D. Wood, P. Zelenay, K. More, K. Stroh, T. Zawodzinski, J. Boncella, J.E. McGrath, M. Inaba, K. Miyatake, M. Hori, K. Ota, Z. Ogumi, S. Miyata, A. Nishikata, Z. Siroma, Y. Uchimoto, K. Yasuda, K.I. Kimijima, N. Iwashita, *Chem. Rev.* 107 (2007) 3904–3951.
- [5] H. Chang, S.H. Joo, C.H. Pak, *J. Mater. Chem.* 17 (2007) 3078–3088.
- [6] Y.Y. Shao, J. Lin, Y. Wang, Y.H. Lin, *J. Mater. Chem.* 19 (2009) 46–59.
- [7] E.P. Ambrosio, C. Francia, M. Manzoli, N. Penazzi, P. Spinelli, *Int. J. Hydrogen Energy* 33 (2008) 3142–3145.
- [8] G. Liu, X. Li, P. Ganesan, B.N. Popov, *Appl. Catal. B: Environ.* 93 (2009) 156–165.
- [9] C.H. Choi, S.Y. Lee, S.H. Park, S.I. Woo, *Appl. Catal. B: Environ.* 103 (2011) 362–368.
- [10] S.G. Ramos, M.S. Moreno, G.A. Andreasen, W.E. Triaca, *Int. J. Hydrogen Energy* 35 (2010) 5925–5929.
- [11] E.B. Fox, H.R. Colon-Mercado, *Int. J. Hydrogen Energy* 35 (2010) 3280–3286.
- [12] G. Gupta, D.A. Slanac, P. Kumar, J.D. Wiggins-Camacho, J. Kim, R. Ryoo, K.J. Stevenson, K.P. Johnston, *J. Phys. Chem. C* 114 (2010) 10796–10805.
- [13] R. Kobayashi, J. Ozaki, *Catal. Lett.* 28 (2009) 396–397.
- [14] C.G. Chung, L. Kim, Y.W. Sung, J. Lee, J.S. Chung, *Int. J. Hydrogen Energy* 34 (2009) 8974–8981.
- [15] G. Perez, E. Pastor, C.F. Zinola, *Int. J. Hydrogen Energy* 34 (2009) 9523–9530.
- [16] Y.K. Zhou, K. Neyerlin, T.S. Olson, S. Pylypenko, J. Bult, H.N. Dinh, T. Gennett, Z.P. Shao, R. O'Hayre, *Energy Environ. Sci.* 3 (2010) 1437–1446.
- [17] P. Nekooi, M. Akbari, M.K. Amini, *Int. J. Hydrogen Energy* 35 (2010) 6392–6398.
- [18] W.M. Wang, Q.H. Huang, J.Y. Liu, Z.Q. Zou, Z.L. Li, H. Yang, *Electrochem. Commun.* 10 (2008) 1396–1399.
- [19] F. Wen, U. Simon, *Chem. Mater.* 19 (2007) 3370–3372.
- [20] J. Zhang, K. Sasaki, E. Sutter, R.R. Adzic, *Science* 315 (2007) 220–222.
- [21] S. Kundu, T.C. Nagaiah, W. Xia, Y. Wang, S.V. Dommele, J.H. Bitter, M. Santa, G. Grundmeier, M. Bron, W. Schuhmann, M. Muhler, *J. Phys. Chem. C* 113 (2009) 14302–14310.
- [22] W. He, Mei Chen, Z.Q. Zou, Z.L. Li, X.G. Zhang, S.-A. Jin, D.J. You, C.H. Pak, H. Yang, *Appl. Catal. B: Environ.* 97 (2010) 347–353.
- [23] W.C. Choi, S.I. Woo, M.K. Jeon, J.M. Sohn, M.R. Kim, H.J. Jeon, *Adv. Mater.* 17 (2005) 446–451.
- [24] G. Selvarani, S.V. Selvaganesh, S. Krishnamurthy, G.V.M. Kiruthika, P. Sridhar, S. Pitchumani, A.K. Shukla, *J. Phys. Chem. C* 113 (2009) 7461–7468.
- [25] W. Chen, J.M. Kim, S.H. Sun, S.W. Chen, *J. Phys. Chem. C* 112 (2008) 3891–3898.
- [26] J. Zhang, H.Z. Yang, K.K. Yang, J. Fang, S.Z. Zou, Z.P. Luo, H. Wang, I.T. Bae, D.Y. Jung, *Adv. Funct. Mater.* 20 (2010) 3727–3733.
- [27] J.R.C. Salgado, E. Antolini, E.R. Gonzalez, *Appl. Catal. B: Environ.* 57 (2005) 283–290.
- [28] P. Hernández-Fernández, S. Rojas, P. Ocón, J.L.G. de la Fuente, P. Terreros, M.A. Peña, J.L. García-Fierro, *Appl. Catal. B: Environ.* 77 (2007) 19–28.
- [29] F.J. Lai, W.N. Su, L.S. Sarma, D.G. Liu, C.A. Hsieh, J.F. Lee, B.J. Hwang, *Chem. Eur. J.* 16 (2010) 4602–4611.
- [30] F.H.B. Lima, J.R.C. Salgado, E.R. Gonzalez, E.A. Ticianelli, *J. Electrochem. Soc.* 154 (2007) A369–A375.
- [31] J. Zhao, A. Manthiram, *Appl. Catal. B: Environ.* 101 (2011) 660–668.
- [32] R.C. Koffi, C. Coutanceau, E. Garnier, J.-M. Léger, C. Lamy, *Electrochim. Acta* 50 (2005) 4117–4127.
- [33] M. Min, J. Cho, K. Cho, H. Kim, *Electrochim. Acta* 45 (2000) 4211–4217.
- [34] S. Takenaka, A. Hirata, E. Tanabe, H. Matsune, M. Kishida, *J. Catal.* 274 (2010) 228–238.
- [35] N. Travitsky, T. Ripenbein, D. Golodnitsky, Y. Rosenberg, L. Burshtein, E. Peled, *J. Power Sources* 161 (2006) 782–789.
- [36] Y. Qian, W. Wen, P.A. Adcock, Z. Jiang, N. Hakim, M.S. Saha, S. Mukerjee, *J. Phys. Chem. C* 112 (2008) 1146–1157.
- [37] S.C. Zignani, E. Antolini, E.R. Gonzalez, *J. Power Sources* 182 (2008) 83–90.
- [38] D. Zhao, J. Feng, Q. Huo, N. Melosh, G.H. Fredrickson, B.F. Chmelka, G.D. Stucky, *Science* 279 (1998) 548–552.
- [39] F.A. Stern, M. Newville, B. Ravel, Y. Yacoby, D. Haskel, *Physica B* 208 (1995) 117–120.
- [40] S. Zabinsky, J.J. Rehr, A.L. Ankudinov, R.C. Albers, M. Eller, *J. Phys. Rev. B* 52 (1995) 2995–3009.
- [41] H.J. Shin, R. Ryoo, M. Kruk, M. Jaroniec, *Chem. Commun.* 34 (2001) 9–350.
- [42] L. Vegard, *Z. Phys.* 5 (1921) 17–26.
- [43] F.H.B. Lima, W.H. Lizcano-Valbuena, E. Teixeira-Neto, F.C. Nart, E.R. Gonzalez, E.A. Ticianelli, *Electrochim. Acta* 52 (2006) 385–393.
- [44] M.T. Bore, H.N. Pham, T.L. Ward, A.K. Datye, *Chem. Commun.* 262 (2004) 0–2621.
- [45] M.T. Bore, H.N. Pham, E.E. Switzer, T.L. Ward, A. Fukuoka, A.K. Datye, *J. Phys. Chem. B* 109 (2005) 2873–2880.
- [46] H. Darmstadt, C. Roy, S. Kaliaguine, T.-W. Kim, R. Ryoo, *Chem. Mater.* 15 (2003) 3300–3307.
- [47] B. Sakintuna, Y. Yürüm, *Ind. Eng. Chem. Res.* 44 (2005) 2893–2902.
- [48] T. Toda, H. Igarashi, H. Uchida, M. Watanabe, *J. Electrochem. Soc.* 146 (1999) 3750–3756.
- [49] X. Zhang, K.-Y. Chan, *Chem. Mater.* 15 (2003) 451–459.
- [50] Z.L. Liu, X.Y. Ling, B. Guo, L. Hong, J.Y. Lee, *J. Power Sources* 167 (2007) 272–280.
- [51] J. Prabhuram, T.S. Zhao, Z.X. Liang, R. Chen, *Electrochim. Acta* 52 (2007) 2649–2656.
- [52] D.R. Rolison, P.L. Hagans, K.E. Swider, J.W. Long, *Langmuir* 15 (1999) 774–779.
- [53] S. Mukerjee, S. Srinivasan, M.P. Soriaga, J. McBreen, *J. Electrochem. Soc.* 142 (1995) 1409–1422.
- [54] J.R.C. Salgado, E. Antolini, E.R. Gonzalez, *J. Power Sources* 138 (2004) 56–60.
- [55] B.J. Hwang, S.M.S. Kumar, C.-H. Chen, Monalisa, M.-Y. Cheng, D.-G. Liu, J.-F. Lee, *J. Phys. Chem. C* 111 (2007) 15267–15276.
- [56] F.J. Lai, L.S. Sarma, H.-L. Chou, D.-G. Liu, C.-A. Hsieh, J.-F. Lee, B.-J. Hwang, *J. Phys. Chem. C* 113 (2009) 12674–12681.
- [57] B.J. Hwang, L.S. Sarma, G.-R. Wang, C.-H. Chen, D.-G. Liu, H.-S. Sheu, J.-F. Lee, *Chem. Eur. J.* 13 (2007) 6255–6264.
- [58] B.J. Hwang, L.S. Sarma, J.-M. Chen, C.-H. Chen, S.-C. Shih, G.-R. Wang, D.-G. Liu, J.-F. Lee, M.-T. Tang, *J. Am. Chem. Soc.* 127 (2005) 11140–11145.
- [59] B.J. Hwang, C.-H. Chen, L.S. Sarma, J.-M. Chen, S.-C. Shih, G.-R. Wang, M.-T. Tang, D.-G. Liu, J.-F. Lee, *J. Phys. Chem. B* 110 (2006) 6475–6482.
- [60] S. Zhang, Y. Shao, G. Yin, Y. Lin, *Appl. Catal. B: Environ.* 102 (2011) 372–377.
- [61] S.-H. Liu, J.-R. Wu, *Int. J. Hydrogen Energy* 36 (2011) 87–93.
- [62] S.-Y. Ang, D.A. Walsh, *Appl. Catal. B: Environ.* 98 (2010) 49–56.
- [63] H.A. Gasteiger, N.M. Markovic, P.N. Ross Jr., E.J. Cairns, *J. Phys. Chem.* 98 (1994) 617–625.
- [64] X.G. Li, I.-M. Hsing, *Electrochim. Acta* 52 (2007) 5462–5469.
- [65] Z.H. Wen, J. Liu, J.H. Li, *Adv. Mater.* 20 (2008) 743–747.